Fiber-optic observations of internal waves and tides

E.F. Williams[1,*], A. Ugalde[2], H. F. Martins[3], C. E. Becerril[4,5], J. Callies[6], M. Claret[2], M. R. Fernandez-Ruiz[4], M. Gonzalez-Herraez[4], S. Martin-Lopez[4], J. L. Pelegri[2], K. B. Winters[7], Z. Zhan[1]

[1]Seismological Laboratory, California Institute of Technology, Pasadena, CA, USA
[2]Institute of Marine Sciences, ICM-CSIC, Barcelona, Spain
[3]Instituto de Optica, CSIC, Madrid, Spain
[4]Department of Electronics, Polytechnic School, University of Alcalá, Alcalá de Henares, Spain
[5]Université Côte d'Azur, CNRS, Observatoire de la Côte d'Azur, IRD, Géoazur, France
[6]Environmental Science and Engineering, California Institute of Technology, Pasadena, CA, USA
[7]Scripps Institution of Oceanography, University of California, San Diego, La Jolla, CA, USA
[*]Now at: Department of Earth and Space Sciences, University of Washington, Seattle, WA, USA

Corresponding author: Ethan Williams (`efwillia@uw.edu`)

This is a non-peer reviewed preprint submitted to *EarthArXiv* and is under review in *Journal of Geophysical Research: Oceans.*

Fiber-optic observations of internal waves and tides

E. F. Williams[1,8], A. Ugalde[2], H. F. Martins[3], C. E. Becerril[4,5], J. Callies[6], M. Claret[2], M. R. Fernandez-Ruiz[4], M. Gonzalez-Herraez[4], S. Martin-Lopez[4], J. L. Pelegri[2], K. B. Winters[7], Z. Zhan[1]

[1]Seismological Laboratory, California Institute of Technology, Pasadena, CA, USA
[2]Institute of Marine Sciences, ICM-CSIC, Barcelona, Spain
[3]Instituto de Optica, CSIC, Madrid, Spain
[4]Department of Electronics, Polytechnic School, University of Alcalá, Alcalá de Henares, Spain
[5]Université Côte d'Azur, CNRS, Observatoire de la Côte d'Azur, IRD, Géoazur, France
[6]Environmental Science and Engineering, California Institute of Technology, Pasadena, CA, USA
[7]Scripps Institution of Oceanography, University of California, San Diego, La Jolla, CA, USA
[8]Now at: Department of Earth and Space Sciences, University of Washington, Seattle, WA, USA

Key Points:

- Distributed acoustic sensing on seafloor cables can resolve temperature changes associated with internal wave and boundary layer dynamics.
- We show temperature transients from solitons in the Strait of Gibraltar and bore-like propagation of the internal tide at Gran Canaria.
- We also recover a signal proportional to barotropic tidal pressure including the fortnightly variation.

Corresponding author: Ethan F. Williams, `efwillia@uw.edu`

Abstract

Although typically used to measure dynamic strain from seismic and acoustic waves, Rayleigh-based distributed acoustic sensing (DAS) is also sensitive to temperature, offering longer range and higher sensitivity to small temperature perturbations than conventional Raman-based distributed temperature sensing. Here, we demonstrate that ocean-bottom DAS can be employed to study internal wave and tide dynamics in the bottom boundary layer, a region of enhanced ocean mixing but scarce observations. First, we show temperature transients up to about 4 K from a power cable in the Strait of Gibraltar south of Spain, associated with passing groups of internal solitary waves in water depth <200 m. Second, we show the bore-like propagation of the nonlinear internal tide on the near-critical slope of the island of Gran Canaria, off the coast of west Africa, with perturbations up to about 2 K at 1-km depth and 0.2 K at 2.5-km depth. With spatial averaging, we also recover a signal proportional to the barotropic tidal pressure, including the lunar fortnightly variation. In addition to applications in observational physical oceanography, our results suggest that contemporary chirped-pulse DAS possesses sufficient long-period sensitivity for seafloor geodesy and tsunami monitoring if ocean temperature variations can be separated.

Plain Language Summary

Distributed acoustic sensing, or DAS, measures changes in the propagation time of light along finite segments of an optical fiber, which can be caused by both elastic deformations and temperature variations. We present two case studies of long-period temperature signals recorded with DAS on submarine cables offshore southern Spain and in the Canary Islands. These temperature signals are associated with internal waves, gravity waves that propagate on the ocean's density stratification. We also recover a signal matching the tidal pressure, which likely represents elastic strain, suggesting potential value of ocean-bottom DAS for seafloor geodesy and tsunami monitoring.

1 Introduction

Internal gravity waves generated by tides, currents, and atmospheric forcing mediate the intensity of ocean mixing, with broad implications for circulation, climate, and biogeochemistry. Early work by Munk (1966), Garrett and Munk (1972), and others proposed that mixing is primarily accomplished through nonlinear interactions and breaking of topographically generated internal waves distributed throughout the ocean interior. However, over the past three decades, observational campaigns have found that the most vigorous mixing occurs near the bottom at sloping boundaries and in regions of rough bathymetry, and that rates of turbulent dissipation vary by at least two orders of magnitude (e.g., Toole et al. (1994); Polzin et al. (1997); Ledwell et al. (2000); Moum et al. (2002); Rudnick et al. (2003); Kunze et al. (2012); Waterhouse et al. (2014)). Yet, observations of internal wave-driven ocean mixing remain exceedingly sparse, especially in the bottom boundary layer. Moored and towed thermistor arrays, current meters, and microstructure profilers can provide high-resolution, local estimates of diapycnal diffusivity and turbulent dissipation rates (e.g. Toole et al. (1994); van Haren (2006)). Global budgets of internal wave generation and dissipation can be constructed by compiling many such in-situ measurements (Waterhouse et al., 2014; Kunze, 2017) or through satellite altimetry (Egbert & Ray, 2000, 2001). Reconciling internal wave and boundary layer dynamics across the vast gulf in scales from astronomical forcing to turbulent dissipation and understanding the physical processes governing the generation and distribution of turbulence are outstanding theoretical and observational challenges, especially for the parameterization of mixing in ocean circulation models.

Distributed fiber-optic sensing offers a promising new approach to observe internal wave dynamics at the seafloor by converting a fiber-optic cable into a dense array of high-resolution temperature sensors. Recently, Connolly and Kirincich (2019), Davis et al. (2020), and others have demonstrated the value of distributed temperature sensing (DTS) for studying shoaling internal waves. Most DTS systems use the intensity of Raman scattering from a repeated laser pulse to estimate temperature along a fiber and are insensitive to other variables like fiber strain. With proper calibration (e.g. Sinnett et al. (2020)), DTS offers absolute temperature measurements with a sensitivity of about 0.01 K and sub-meter sampling up to a range of 10–30 km (Li & Zhang, 2022). However, DTS suffers from a trade-off between distance and sensitivity, which limits its application to shallow water environments insomuch as the DTS laser interrogator must remain onshore. Further, DTS is best suited for multi-mode fiber, which means that pre-existing ocean-bottom telecommunication “dark” fiber cannot be easily repurposed as temperature sensing arrays because it is mostly single-mode. Another fiber-optic sensing technology, distributed acoustic sensing (DAS) uses the phase of Rayleigh-scattered laser light to estimate changes in the optical path length, which can be caused by both temperature and elastic deformation with an equivalence of 1 K $\approx$ 10 $\mu\varepsilon$ (where $1\mu\varepsilon = 10^{-6}$ m/m) (Fernandez-Ruiz et al., 2020; Lindsey & Martin, 2021). At short periods (<50-100 s) or in shallow water (<100-200 m), mechanical strain from ocean surface gravity, acoustic, and seismic waves always dominates over temperature effects, permitting diverse applications of ocean-bottom DAS from earthquake detection and structural characterization of the seafloor (Sladen et al., 2019; Cheng et al., 2021; Williams et al., 2021) to monitoring sea state and tracking coastal currents (Lindsey et al., 2019; Williams et al., 2019, 2022). However, at long periods or in deep water, temperature transients associated with internal waves and tides may rise to the fore. Ide et al. (2021) first reported complex temperature signals at tidal periods in ocean-bottom DAS measurements offshore Cape Muroto in southern Japan. With a field sensitivity of about $0.001-0.01\mu\varepsilon = 0.1-1$ mK, DAS is actually more sensitive to small temperature signals than DTS and can operate up to 100 km without significant reduction in sensitivity, permitting oceanographic investigations at abyssal depths where temperature anomalies are small. However, DAS faces several challenges of its own: temperature and mechanical strain effects cannot be definitively separated in a single measurement, temperature calibrations for DAS have not yet been standardized, and the instrumental noise increases with period on most DAS systems.

Here, we present two novel observations of internal wave dynamics from ocean-bottom DAS arrays. In Section 3, we show temperature perturbations up to about 4 K associated with internal solitary waves crossing a power-cable in the Strait of Gibraltar, south of Spain. In Section 4, we show temperature perturbations up to about 2 K associated with nonlinear, bore-like propagation of the internal tide on the near-critical slope of Gran Canaria, in the Canary Islands offshore west Africa. Throughout, we assume that these long-period signals solely represent temperature, an assumption which we then discuss and justify in Section 5.

2 Data

We analyze and compare observations from two DAS datasets acquired on seafloor cables containing optical fibers. The first was recorded in October 2019 on a 30-km power cable running from Spain to Morocco across the Strait of Gibraltar, with depths up to about 550 m (Figure 1A). The cable is generally buried on the Spanish shelf, and emerges

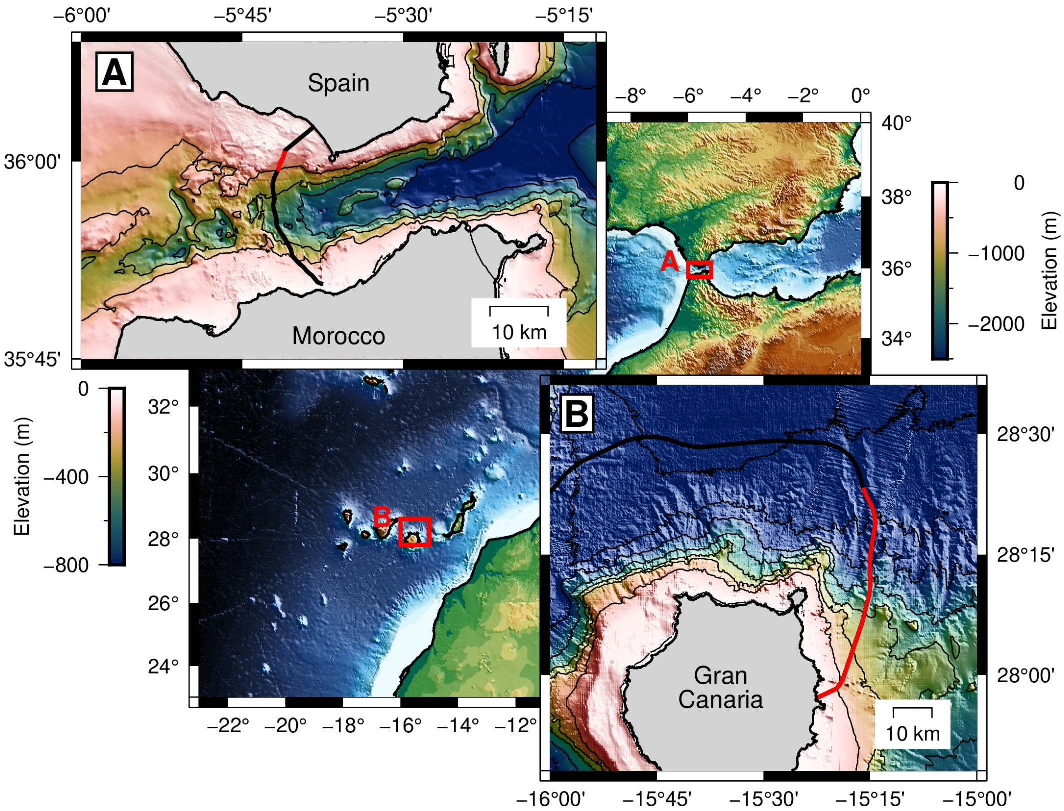

Figure 1. Map of cable locations. (A) Power cable from Spain to Morocco across the Strait of Gibraltar (black) with section shown in Figure 2 in red; 200-m bathymetry contours (B) Telecommunications cable from Gran Canaria to Tenerife (black) with section shown in Figure 3 in red; 1000-m bathymetry contours.

at the seafloor at 8.6 km optical distance. The second was recorded in August and September 2020 on a 176-km telecommunication cable connecting Gran Canaria to Tenerife in the Canary Islands, with depths up to about 4 km (Figure 1B). The cable is entirely unburied beyond the surf zone. Fibers in both cables were interrogated with a chirped-pulse DAS system built by Aragon Photonics and operated by the University of Alcala (Pastor-Graells et al., 2016; Fernandez-Ruiz et al., 2018, 2019), using a 10-m gauge length and 10-m channel spacing. The raw DAS data were first decimated from 1 kHz to 1 Hz by averaging. A five-point median filter was applied to the 1-Hz data to prevent instrumental noise like spikes and steps from biasing long period results, and then the data were further decimated to 100 s sampling period. For more information, see Williams et al. (2022) and Ugalde et al. (2022).

3 Internal solitary waves in the Strait of Gibraltar

3.1 Observations

Four days from the Strait of Gibraltar DAS dataset are plotted in Figure 2. Across the buried section of the cable, there is no evident temperature signal at any period. Emerging abruptly at 8.6 km where the cable is exposed at the seafloor, a nearly constant background temperature is periodically broken by positive excursions up to 4 K, indicative of internal waves of depression. Each internal wave group lasts 2-8 h and is composed of 2–6 subsidiary solitary waves, each with a period of 1–2 h (Figure 2B,D). These excursions occur twice daily immediately following the maximum eastward tidal flow and exhibit an oscillation in amplitude which correlates with the daily inequality of the diurnal and semidiurnal tides as expressed in the TPXO9 shallow-water solution for the local barotropic current (Figure 2C) (Egbert & Erofeeva, 2002). The amplitude is strongest where the cable emerges at 8.6 km distance (75 m depth) and decays monotonically with distance, disappearing before the 11-km mark (200 m depth).

3.2 Interpretation

Hydrodynamics in the Strait of Gibraltar are characterized by a two-layer exchange flow between salty Mediterranean water at the bottom and less-salty Atlantic water at the surface, with a strong pycnocline typically measured at 50-100 m depth near the cable location east of the Camarinal Sill. Modulation of the exchange by tidal currents re-

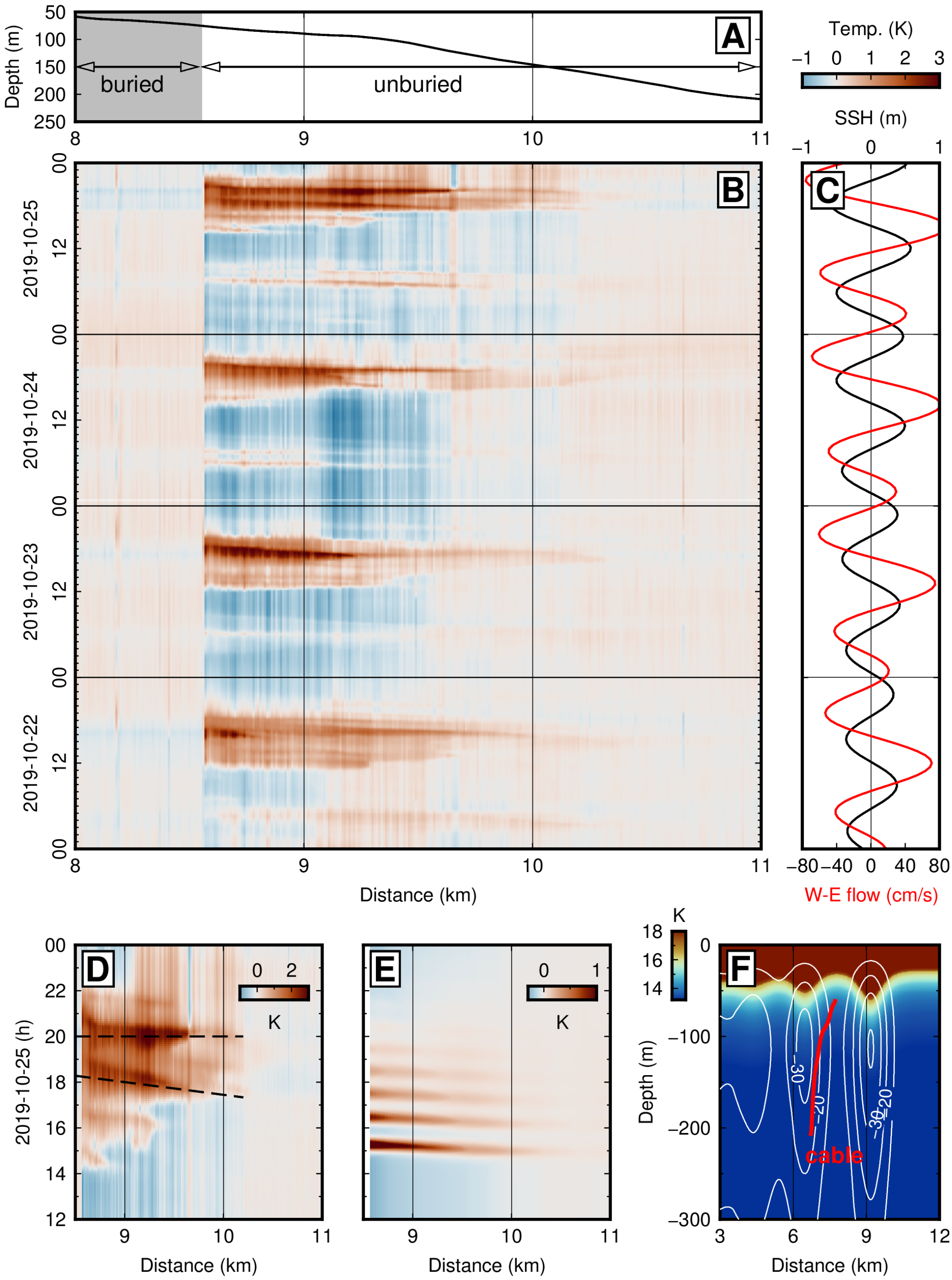

Figure 2. Internal solitary wave groups on the Gibraltar cable. (A) Cable bathymetry profile with shading to indicate burial. (B) DAS data from 2019-10-22 to 2019-10-25 for the 8–11-km cable section. (C) Tidal predictions for sea surface height (SSH, black) and meridional flow (red) from TPXO. (D) Zoom-in to panel B showing a group of internal solitons, with dashed black lines schematically indicating the difference in moveout (apparent speed) between individual solitons. (E) Synthetic data generated using the "dnoidal" model of Apel (2003) for the 8–11-km cable with a source at the north end of Camarinal Sill on the Spanish shelf. (F) Cross-section of the model after Apel (2003) at $T = 4$ h with absolute temperature, contours of constant isopycnal displacement (white lines), and depth vs. distance from source for the 8–11-km cable segment (red).

sults in partial blocking of the Mediterranean outflow over the Camarinal Sill and the generation of internal solitary waves, which propagate eastward into the Alboran Sea and have been widely observed by moorings and in synthetic aperture radar (SAR) imagery (Brandt et al., 1996; Vazquez et al., 2008; Ziegenbein, 1969, 1970; Watson & Robsinson, 1990). Although no clear SAR images of internal waves were acquired during the four-day data window, the Sentinel-1A satellite captured an internal wave group propagating past Gibraltar at 2019-10-26 06:27:44 UTC, shortly after the end of DAS acquisition (Figure S1A). This likely corresponds to the wave group shown in Figure 2D and confirms that this well-studied phenomenon occurred during our experiment.

In order to understand the relationship between internal wave parameters and the temperature signals recorded in DAS data, we compare our observations with synthetic data generated from the "dnoidal" model of Apel (2003) (Figure 2E,F), which combines an analytical solution of the Korteweg-de Vries equation for weakly-nonlinear solitary wave propagation with a vertical structure function obtained by numerical solution of the Taylor-Goldstein equation (see Text S1). While the observed inter-soliton period and group shape are poorly reproduced by this simplistic model, the synthetic data match the amplitude of the temperature anomaly within a factor of two and mimic its quasi-triangular shape with depth and distance (Figure 2D,E). The DAS temperature observations can consequently be understood as an oblique cross-sectional slice of the internal wave group along the cable trajectory, where the shape is governed by a combination of the isotherm displacement with the thermal stratification, and the moveout is determined by the source azimuth and propagation speed (Figure 2F). Though the moveout along the cable varies slightly from one solitary wave to the next, suggesting a complex source distribution (see dashed lines in Figure 2D), the apparent speed of propagation along the cable direction is almost instantaneous, which requires broad-side incidence of the internal wave group and a source at the northern end of the Camarinal Sill or on the Spanish shelf (Figure S2). The ESE-ward propagation perpendicular to the cable azimuth that would result from a dominant source at the northern end of the Camarinal Sill is supported by SAR imagery (Figure S1B, see also Brandt et al. (1996) Figure 16B). However, given trade-offs between speed, source time, and source location as well as refraction across the steep bathymetry, it is impossible to uniquely identify the source without more elaborate modeling.

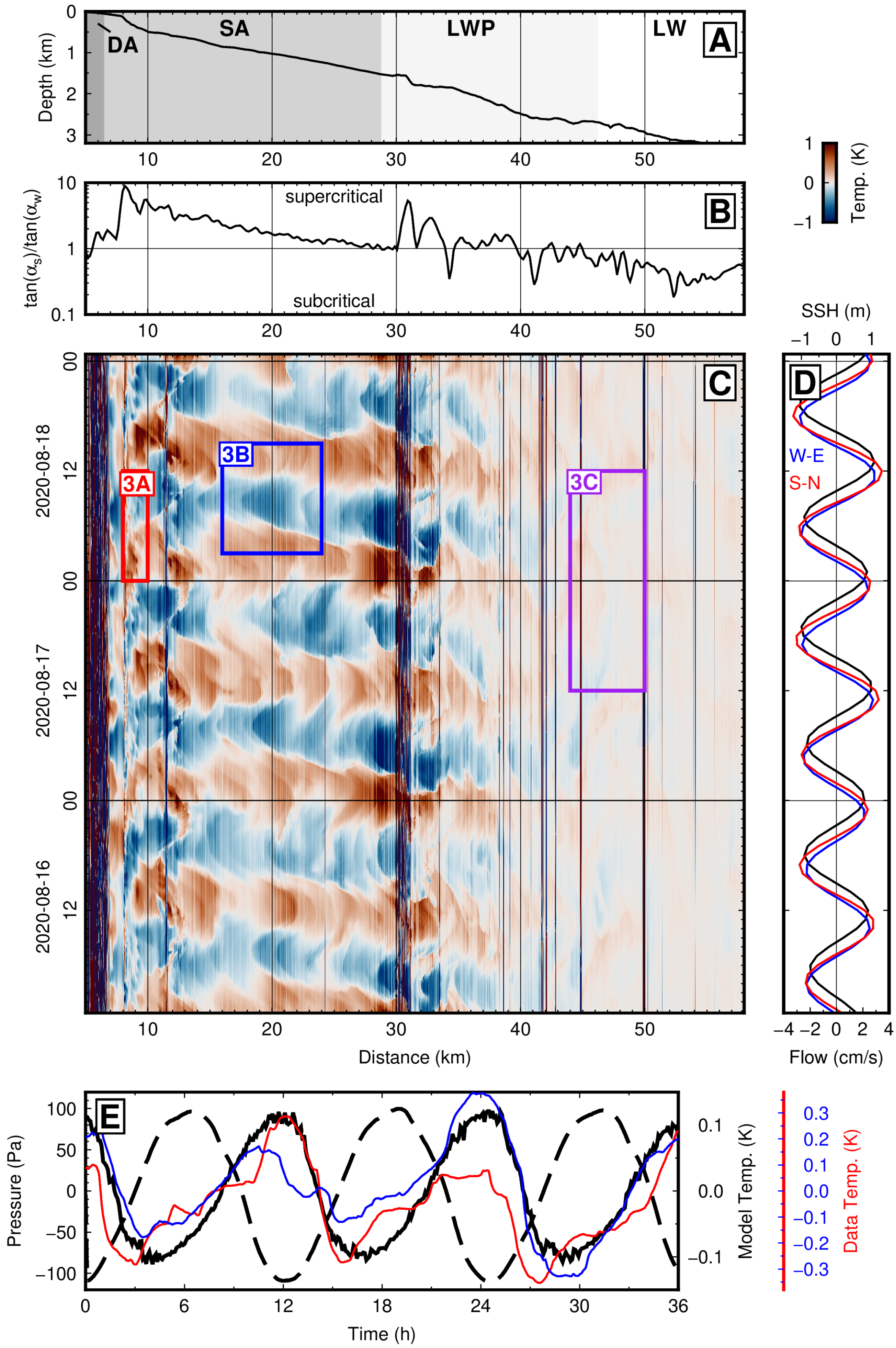

Figure 3. Nonlinear internal tide on the slope of Gran Canaria. (A) Cable bathymetry profile with shading to indicate cable type: double armored (DA), single armored (SA), light-weight protected (LWP), and light-weight (LW). (B) Slope criticality along the cable profile, defined as the ratio of the absolute slope angle to the angle of internal wave energy propagation. (C) DAS data from 2020-08-16 to 2020-08-18 for the 5–58 km cable section. (D) Tidal predictions for sea surface height (black), meridional flow (blue), and zonal flow (red) from TPXO. (E) Comparison of DAS observations at 22 km (red) and 28 km (blue) with modeled temperature (black solid) and pressure (black dashed) perturbations.

4 Nonlinear internal tides at Gran Canaria

4.1 Observations

Three days from the Gran Canaria DAS dataset are plotted in Figure 3, showing semidiurnal temperature oscillations up to 2 K in amplitude which persist along the entire slope spanning a depth range >3 km. The observations can generally be divided into three domains. On the main slope of Gran Canaria (12–30 km distance, 500–1500 m depth) three to five sharp cold fronts form every 12 hrs (Figure 3C, 4B; Movie S1). Here, the slope is slightly supercritical, with $1 \leq \gamma \leq 3$, where $\gamma = \tan(\alpha_s)/\tan(\alpha_w)$ is the ratio of the bathymetric slope angle (α_s) to the angle of internal wave energy propagation (α_w, Figure 3B). As these fronts form and accelerate up to an apparent velocity of 0.5 m/s along the cable, they intensify to a contrast in excess of 1 K over a distance of only a few hundred meters. Then, as the tidal flow reverses direction, the cold fronts slow, dissipate, and reform into a series of weaker warm fronts that recede down the slope. In shallow water (7–12 km distance, <500 m depth, $\gamma > 3$), the shoaling cold fronts slow to an apparent velocity of 0.1 m/s and divide into 5-10 weaker fronts across each semidiurnal cycle (Figure 4A). Beyond a sharp ridge at 30-km distance, the seafloor fabric is much rougher and the flow pattern more complex, but sharp temperature fronts up to about 0.2 K still persist and are advected horizontally by the tidal current (Figure 4C).

4.2 Interpretation

Steep submarine topography acts as both a source for the conversion of barotropic tidal motions into internal waves and a sink where the internal tide reflects and breaks, thus mediating the cascade of energy in the ocean from large to small scales where mixing occurs (Klymak et al., 2011; St. Laurent & Garrett, 2002; Rudnick et al., 2003). High-resolution thermistor observations and modeling of steep, near-critical slopes have shown that the generation and shoaling of the internal tide drives the formation and propagation of bore-like fronts in the bottom boundary layer (van Haren, 2006; Winters, 2015) associated with intensified turbulent mixing and shear instability (van Haren & Gostiaux, 2012; van Haren et al., 2015; van Haren & Gostiaux, 2010). These observations are broadly consistent with the temperature oscillations in DAS data from Gran Canaria, including frontal velocities in the range 0.1–0.5 m/s and temperature perturbations up to 3 K at 500-m depth (van Haren & Gostiaux, 2012), 2 K at 1400-m depth (van Haren,

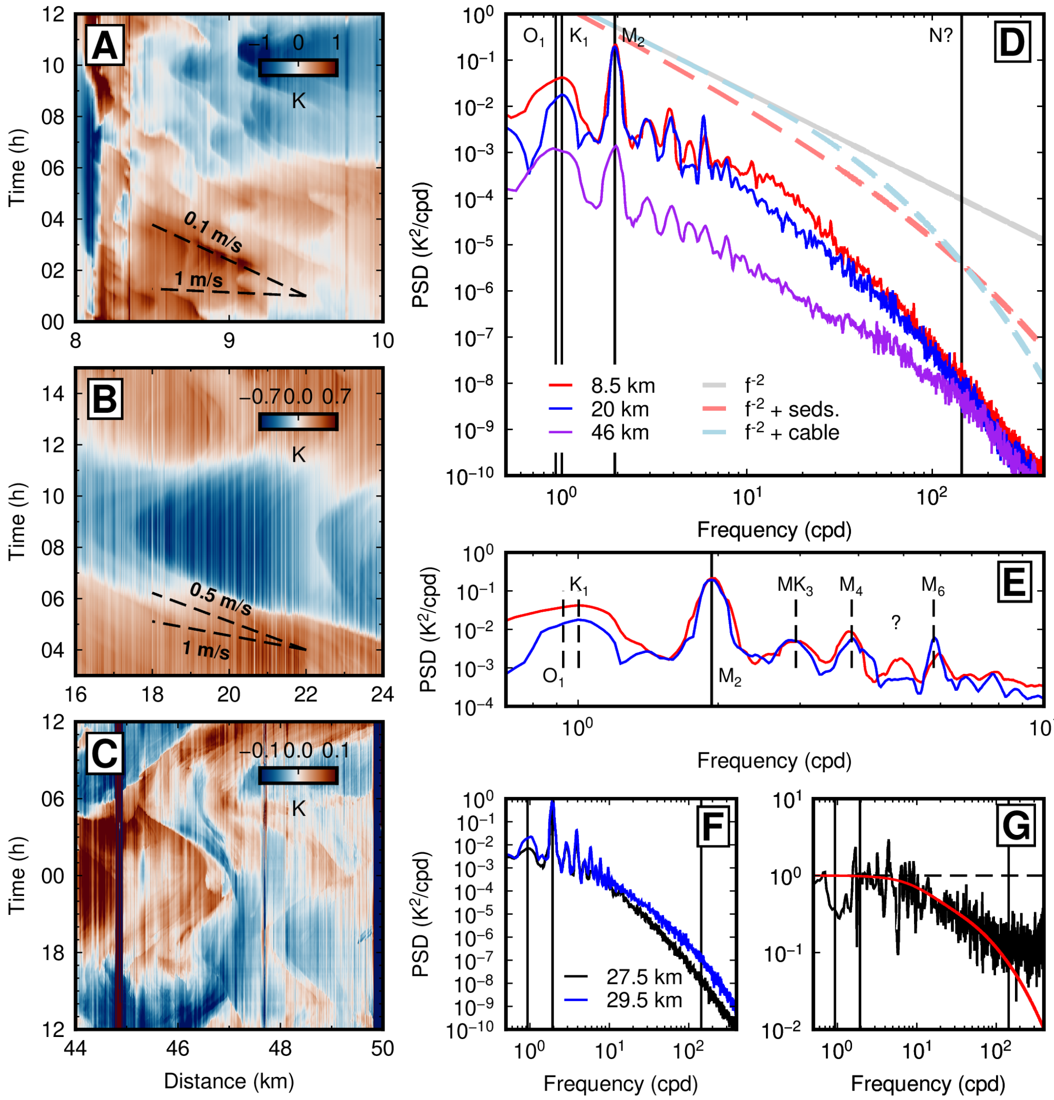

Figure 4. (A) Zoom-in to the 8–10-km cable segment of the Gran Canaria dataset showing many small cold fronts shoaling on the shallow shelf. (B) Zoom-in to the 16–24-km cable segment showing a sharp cold front propagating up slope, slowing around 18-km, and reversing or breaking. (C) Zoom-in to the 44–50-km cable segment showing complex, sharp temperature fronts oscillating at tidal periods. (D) Thirty-day power spectral density (PSD) for a representative channel from each panel of A,B,C, compared with a reference slope of f^{-2} and dashed lines illustrating the effect of burial (light red) or cable thickness (light blue) on the frequency-dependent temperature response. (E) Zoom-in to D showing the ordinary tidal harmonics (O_1, K_1, M_2) and nonlinear overtones (MK_3, M_4, M_6) present at all water depths. (F) Spectra for two channels on either side of the single-armored to light-weight protected cable transition, showing a frequency-dependent difference in response. (G) Transfer function between the two channels in F (black line) and simple thermal model based on the actual difference in cable diameter (red line).

2006), and 0.2 K at 2500-m depth. (van Haren et al., 2015). The observed pattern of the shoaling, weakening, and reversal of bore-like fronts is similar to signals observed in very shallow water with DTS at Dongsha Atoll, which Davis et al. (2020) termed "relaxation."

We compare the DAS observations to an idealized simulation of near-boundary flow driven by reflection of a fundamental mode M_2 internal tide across a slightly supercritical sloping bottom, performed using **flow_solve** (Winters & de la Fuente, 2012) and scaled to approximate the conditions at Gran Canaria (see Text S2, Figures S3, S4). Figure 3E plots example DAS records from individual channels at 22 and 28 km distance against differential temperature from a near-bottom point in the simulation, showing a consistent pattern over each tidal cycle of a gradual rise in temperature followed by a sharp drop, marking the passage of an up-slope propagating front. Notably, this asymmetry is not evident in the modeled pressure, which is dominated by vertical displacements of the large-scale, linear internal tide throughout the overlying water column and nearly independent of the near-bottom flow. The modeled temperature perturbations of 0.2–0.3 K are of slightly smaller amplitude than the 0.4–1 K perturbations observed with DAS, which is a reasonable level of agreement considering the idealized simulation was conducted with uniform stratification and only one internal tide mode. The modeled maximum frontal velocity is 0.65 m/s, consistent with the observed 0.5 m/s (Figure S4).

The temperature spectra of individual DAS channels exhibit dominant peaks at semidiurnal (M_2) and diurnal (O_1, K_1) frequencies (Figure 4D,E). At the latitude of Gran Canaria, the inertial frequency is very close to O_1, so the prominence of the diurnal peak could relate to both forcing of the diurnal tide and the presence of near-inertial waves. Also evident are several tidal overtones (MK_3, M_4, etc.), which persist in relative amplitude across the full range of observations, indicating nonlinear interactions on the slope associated with local conversion of the barotropic tide or steepening of the internal tide (van Haren et al., 2002). For the deepest cable segment beyond 40-km distance, the spectrum approximately scales as f^{-2} (Figure 4D), similar to the canonical Garrett-Munk spectrum for internal waves in the ocean interior, away from generation sites (Garrett & Munk, 1972). For the 7–30-km cable segment, the spectrum is flatter from about 1 to 10 cpd, indicative of stronger nonlinearity, approximately scaling as f^{-1}. At higher frequencies, the spectrum steepens beyond f^{-3}, which may reflect diminished temperature sensitivity due to the finite thickness of the cable construction or even a few millimeters of sediment drape (Figure 4D, S5). Comparing adjacent cable segments across the transition from single-armored (SA, 26-mm diameter) to light-weight protected (LWP, 19.6-mm diameter) cable type, there is a frequency-dependent difference in response, which can be adequately described with a simple thermal transfer-function model (Figure 4F,G). Consequently, the spectral slope at high frequencies should probably not be interpreted. For such a model, the phase response of the cable to external thermal forcing is also frequency-dependent and non-negligible, which implies that the sharp temperature fronts observed here may truly be sharper still if observed by a thermistor at the same location (see Text S3, Figure S5).

4.3 Hidden signature of the barotropic tide

While the observation of complex temperature fluctuations with ocean-bottom DAS provides a unique opportunity for study of internal wave and boundary layer dynamics, the large amplitude of these signals poses a significant challenge to observing pressure perturbations and solid-Earth deformations, such as associated with tsunamis and slow earthquakes. Exploiting the fact that the wavelength of the barotropic tide is much greater than the wavelength of the temperature variations associated with the internal tide on a near-critical slope, we compute a spatial median across the 15–30 km cable segment, which is plotted in Figure 5 and compared with the barotropic tidal pressure, estimated from TPXO (Egbert & Erofeeva, 2002). The recovered signal, plotted in units of pressure for the purpose of interpretation, matches the predicted phase of the barotropic tide including the fortnightly variation (M_f), which strongly suggests that this signal represents mechanical strain in the cable due to pressure. The observed amplitude is 2–8 $\mu\varepsilon$ and scales to pressure as $\frac{\varepsilon}{\Delta p} \sim 5 \times 10^{-10}$ Pa^{-1}, which is a plausible value of horizontal seafloor compliance (Crawford et al., 1991) though slightly larger than the predicted strain induced in a cable from hydrostatic pressure perturbations alone (Mecozzi et al., 2021). While we note that this simple averaging procedure does not guarantee the full recovery of the tidally-induced mechanical strain signal or complete elimination of temperature residuals, the demonstrated sensitivity is promising for application of ocean-bottom DAS in seismo-geodesy.

5 Discussion and conclusions

Thus far we have assumed that the long-period transients observed in DAS data from the Strait of Gibraltar and Gran Canaria are dominated by temperature. Conven-

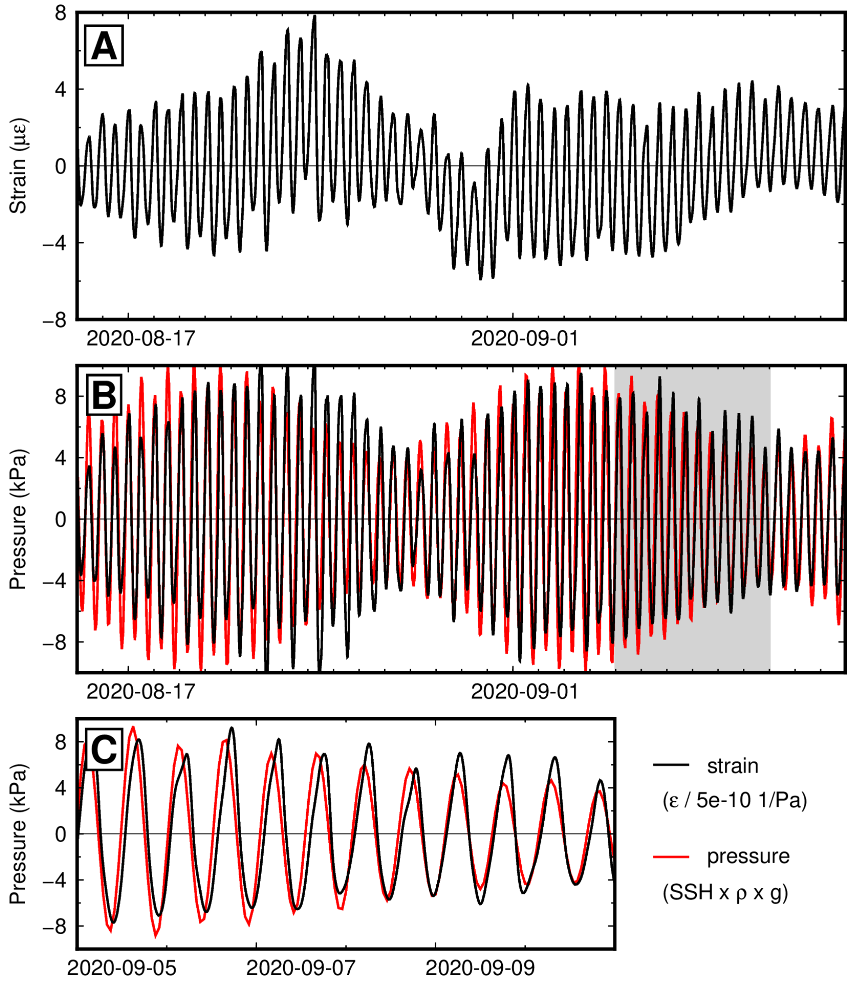

Figure 5. (A) Long-period DAS signal removed by the default laser denoising parameters in units of nanostrain. (B) Same as A with low-pass filter with a corner frequency of 48 h scaled to units of pressure as $p = \varepsilon/(5 \times 10^{-10})$ (black), and barotropic tidal pressure from TPXO (red). (C) Zoom-in to the gray shaded window in B.

tional applications of DAS are, however, as a dynamic strain sensor, and the extraction of a signal proportional to barotropic tidal pressure indicates that mechanical strain is non-negligible. A typical DAS system, such as the chirped-pulse instrument used here (Fernandez-Ruiz et al., 2019), estimates changes in optical path length across each fiber segment by measuring small perturbations in the phase of backscatter between two consecutive laser pulses. For a finite fiber segment of length L, the differential phase is given by:

$$\Delta\phi = \frac{4\pi nL}{\lambda}\left(\frac{\delta L}{L} + \frac{\delta n}{n}\right)$$

where n is the index of refraction and λ is the laser wavelength. Changes in the optical path length measured by DAS can therefore result from mechanical strain or a change in temperature. Both mechanisms include a physical strain $\frac{\delta L}{L}$ and a change in refractive index $\frac{\delta n}{n}$. Letting $\phi = \frac{4\pi nL}{\lambda}$, for mechanical strain ε, $\frac{\Delta\phi}{\phi} = (1+\psi)\varepsilon$, where $\psi \approx -0.22$ accounts for the effect of photoelasticity at $\lambda = 1550$ nm. For a change in temperature ΔT, $\frac{\Delta\phi}{\phi} = (\alpha_T + \xi)\Delta T$, where the thermal expansion coefficient is $\alpha_T \approx 5 \times 10^{-7}$ K^{-1} and the thermo-optic coefficient is $\xi \approx 6.8{\times}10^{-6}$ K^{-1}. Therefore the equivalence between temperature and strain is $\frac{\Delta T}{\varepsilon} \approx 10^5$ K (e.g. Koyamada et al. (2009)). The uncertainty in these parameters is challenging to quantify, since no calibration has been performed in situ, but a factor of two deviation in the strain-to-temperature relation is conceivable. Cable construction and burial can only thermally insulate the fiber, so the conversion used here should otherwise represent the minimum value of relative temperature (Sidenko et al., 2022).

Based on five key points of observation, we assert that the long-period transients described above are predominately if not entirely changes in the temperature of the fiber:

1. A 20–40 $\mu\varepsilon$ strain, equivalent to the 2 K observed at Gran Canaria or 4 K observed in Gibraltar, is simply too large to be physically plausible as mechanical strain, being comparable to the near-field (<1-km epicentral distance) peak strain recorded during the 2019 M7.1 Ridgecrest earthquake (Farghal et al., 2020). Given steel and aluminum elements in the cable construction (Young's modulus 100–200 GPa), such a strain would require an oscillating 10–40 MPa stress, which is comparable to or greater than the weight of the entire water column. Further, the signal observed at Gran Canaria is coherent over a >10-km distance, which would imply an integrated displacement of at least 20 cm every 12 hr across the cable.

2. The sudden disappearance of a 4 K signal at the point of burial of the Gibraltar cable over a distance of one channel (10 m) (Figure 2) can only be attributed to temperature. Any pressure forcing sufficient to deform a cable at the seafloor 40 $\mu\varepsilon$ must be transmitted at a measurable level to a shallowly buried cable, as evidenced by much smaller surface gravity wave pressure signals observed on the buried 3–6-km section of this same cable (Williams et al., 2022). Conversely, thermal signals may be retarded by as little as a few centimeters of sediment, owing to the small thermal diffusivity of geological materials (Figure S5).
3. The observed signature of the nonlinear internal tide at Gran Canaria (Figure 3) is 5–10 times larger than the spatially-averaged signal, the latter of which corresponds with the barotropic tidal pressure (Figure 5). This amplitude ratio is inconsistent with the expectation for pressure-induced mechanical strain from the baroclinic tide, as supported by modeling (Figure 3E, S4). The ocean-bottom pressure perturbation from the barotropic tide (order 1–10 kPa) is larger than that from baroclinic tide (order 10–100 Pa) because the density contrast at the sea surface is about 1000 times larger than the density contrast across the pycnocline, even though isopycnal displacement may be as much as 100 times larger than the sea surface displacement (e.g. Moum and Smyth (2006)). Conversely, the ocean-bottom temperature perturbation from the barotropic tide is negligible, whereas the baroclinic tide can induce >1 K temperature changes even at depths >1 km (e.g. van Haren (2006)).
4. The temporal asymmetry seen in modeled and observed bottom boundary layers over nearly critical slopes, the frontal velocities consistent with bores, together with the lack of asymmetry and much larger wavelength inferred from the corresponding modeled pressure signal, provides oceanographic supporting evidence that DAS measurements are principally responsive to small temperature fluctuations associated with nonlinear boundary layer dynamics rather than to the tidally oscillating bottom pressure (Figure 3,S4).
5. The change in cable type between single-armored and light-weight protected around 29-km on the Gran Canaria cable (Figure 3A) manifests a frequency-dependent change in sensitivity which can be adequately described using a simple thermal model for the difference in cable diameter (Figure 4F,G).

We conclude that the observed long-period transients in both datasets are dominated by temperature effects. However, the relative contributions of strain and temperature may not be simple to identify in most ocean-bottom DAS datasets. In particular, DAS has potential as a seafloor geodetic method for monitoring offshore fault zones, but the solid-Earth strains associated with processes like fault creep and slow earthquakes will likely be smaller than or comparable to oceanic temperature signals from internal tide and boundary layer dynamics along the slopes of active margins. Concurrent measurement with both DAS and DTS may provide one solution, but is limited by the short range of DTS. Another possibility is to utilize bespoke cables with fibers of differing thermal properties so that the temperature signal can be subtracted (Zumberge et al., 2018), but this excludes pre-existing submarine telecommunication cables. Here, we recovered mechanical strain associated with pressure by naive spatial averaging, which was successful owing to the difference in wavelength between the internal and barotropic tides. This suggests that a more general multi-scale approach like principal component analysis might be capable of separating mechanical and thermal signals, as is commonly performed to remove secular and seasonal trends from geodetic time-series.

Our study highlights several other outstanding challenges for fiber-optic oceanography. DAS sensitivity to temperature has not been calibrated in a field environment, and the thermal amplitude and phase response of submarine cables is generally not known. In both the Strait of Gibraltar and Gran Canaria DAS datasets, we observed differences in amplitude between even adjacent channels (see striping or vertical lines on Figures 2, 3, 4) indicating differences in broadband temperature response, which could result from partial burial of the cable with a few millimeters of sediment drape or variations in instrumental sensitivity (Figure S5). Beyond the instrument itself, the novel observation of a continuous horizontal profile of seafloor temperature needs to be reconciled with conventional oceanographic measurements. For example, in-situ comparison with data from current meters and thermistors could help explain whether the dissipation and reversal of temperature fronts on the slope of Gran Canaria is associated with internal wave breaking, and whether the internal tide is being generated locally or remotely. Importantly, without complementary measurements it is not possible to directly calculate the diapycnal diffusivity or other key parameters necessary to quantify the intensity of tidal dissipation and mixing observed here. Until such calibrations and validations are available, the ability of ocean-bottom DAS to leverage widespread, pre-existing submarine telecommunication infrastructure at relatively low cost for monitoring near-bottom dynamics from the abyssal ocean to the shallow shelf may prove most useful for targeted site selection of conventional oceanographic surveys and generalization of local measurements to larger scales.

Data Availability

All 4.5 days of DAS data from the Strait of Gibraltar necessary to reproduce Figure 2 and the 3 days of DAS data from Gran Canaria necessary to reproduce Figures 3 and 4 are available through the CaltechDATA repository (`https://doi.org/10.22002/j8cbw-j1602`).

Acknowledgments

The authors acknowledge Red Electrica de España and CANALINK-Canarias submarine link S.L., part of group Instituto Tecnológico y de Energías Renovables (ITER) and Cabildo de Tenerife, for providing cable access and support during the DAS deployments. Funding for this project was provided through the "Severo Ochoa Centre of Excellence" accreditation (CEX2019-000928-S), the Spanish MCIN/AEI/10.13039/501100011033 and the European Union NextGenerationEU/PRTR Program under projects PSI ref. PLEC2021-007875 and TREMORS ref. CPP2021-008869, the Spanish MCIN/AEI/10.13039/501100011033 and FEDER Program under projects PID2021-128000OB-C21 and PID2021-128000OB-C22, and the European Innovation Council under Grant SAFE: ref. 101098992.

E. F. W. was supported by a National Science Foundation Graduate Research Fellowship. M.C. was funded by the European Union (HORIZON-MSCA-2021-PF MOORING, grant agreement no. 101064423). M. R. F.-R. and H. F. M. acknowledge support from the MCIN/AEI/10.13039/501100011033 and European Union NextGenerationEU/PRTR under grants RYC2021-032167-I and RYC2021-035009-I, respectively. J. C. acknowledges support from the National Science Foundation under Grant No. OCE-2023161. K. B. W. acknowledges funding provided by the U.S. National Science Foundation (grants OCE-2045399 and OCE-185076) and the U.S. Office of Naval Research (grant N00014-18-1-2803). Z. Z. acknowledges support from the Moore Foundation and NSF under CAREER Award 1848166.

The authors declare no conflicts of interest relevant to this study.

Supporting Information for "Fiber-optic observations of internal waves and tides"

E. F. Williams[1,8], A. Ugalde[2], H. F. Martins[3], C. E. Becerril[4,5], J. Callies[6], M. Claret[2], M. R. Fernandez-Ruiz[4], M. Gonzalez-Herraez[4], S. Martin-Lopez[4], J. L. Pelegri[2], K. B. Winters[7], Z. Zhan[1]

[1]Seismological Laboratory, California Institute of Technology, Pasadena, CA, USA
[2]Institute of Marine Sciences, ICM-CSIC, Barcelona, Spain
[3]Instituto de Optica, CSIC, Madrid, Spain
[4]Department of Electronics, Polytechnic School, University of Alcalá, Alcalá de Henares, Spain
[5]Université Côte d'Azur, CNRS, Observatoire de la Côte d'Azur, IRD, Géoazur, France
[6]Environmental Science and Engineering, California Institute of Technology, Pasadena, CA, USA
[7]Scripps Institution of Oceanography, University of California, San Diego, La Jolla, CA, USA
[8]Now at: Department of Earth and Space Sciences, University of Washington, Seattle, WA, USA

Contents of this file

Additional Supporting Information

1. Movies S1

Text S1. A schematic internal wave model after Apel (2003)

In order to understand the relationship between the temperature excursions observed with DAS and internal solitary wave parameters, we constructed synthetic data using the "dnoidal" model of Apel (2003). We first picked a relatively arbitrary source location at the northern end of the Camarinal Sill towards the Spanish shelf (green star in Figure S2A) and calculated the propagation distance for each point along the cable path. Then, we evaluated Apel's model to obtain the isopycnal displacement at each point along the cable as a function of time:

$$\eta(x,z,t;k) = \eta_0 W_k(z) I(x,t)\left[2\mathrm{dn}^2_{s(x)}\left(\frac{1}{2}k_0(x-Vt)\right) - \left(1-s^2(x)\right)\right]$$

Here, $W_k(z)$ is the vertical structure function determined by numerical solution of the Taylor-Goldstein equation given realistic stratification for the Strait of Gibraltar. The

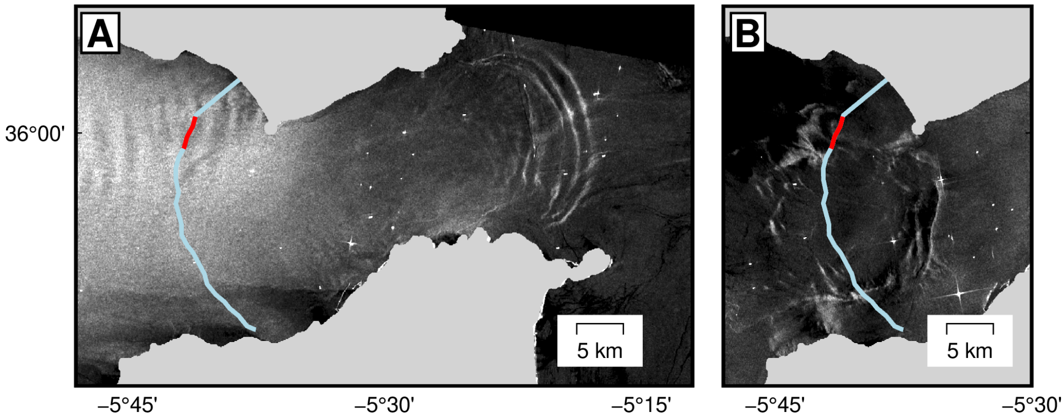

Figure S1. (A) Synthetic aperture radar (SAR) image of the Strait of Gibraltar from Sentinel-1A acquired at 2019-10-26 06:27:44 UTC, showing an internal wave group propagating eastward into the Alboran Sea (normalized color scale). (B) SAR image from Sentinel-1B acquired at 2019-10-02 18:17:43 UTC showing a nascent internal wave group near the cable location propagating ESE, suggestive of a source towards the north of the Strait.

duration and decay of the wave group is given by $I(x,t)$, which is an envelope function. The term $\mathrm{dn}_{s(x)}$ is a Jacobian elliptic function and a solution to the Korteweg-de Vries equation for weakly nonlinear wave propagation. The term $s(x)$ is a shape parameter for the Jacobian elliptic function which determines the dispersion. Apel (2003) provides expressions to evaluate each of these terms along with hyperparameters used by Apel to model SAR images of internal solitary wave propagation in the Strait of Gibraltar. We set the leading-soliton wavelength k at 2-km to match SAR scenes acquired around the time of our experiment (Figure S1) and modified one parameter in I to make the group duration 6-h for comparison with the data. Otherwise, all parameters are as provided by Apel (2003).

Given the model time-series of isopycnal displacement along the cable, we then multiplied the isopycnal displacement by the local temperature gradient $\frac{\partial T}{\partial z}$ using a CTD profile from the 1986 Gibraltar Experiment nearest the cable location (Kinder & Bryden, 1987) in order to obtain the relative temperature at each point. This assumes negligible diapycnal transformation during wave propagation. Previous authors have noted a persistent change in stratification following the passage of internal solitary wave groups in the Strait of Gibraltar (Ziegenbein, 1969), which implies this may be a poor assumption, although the background temperature observed in DAS data is unchanged between

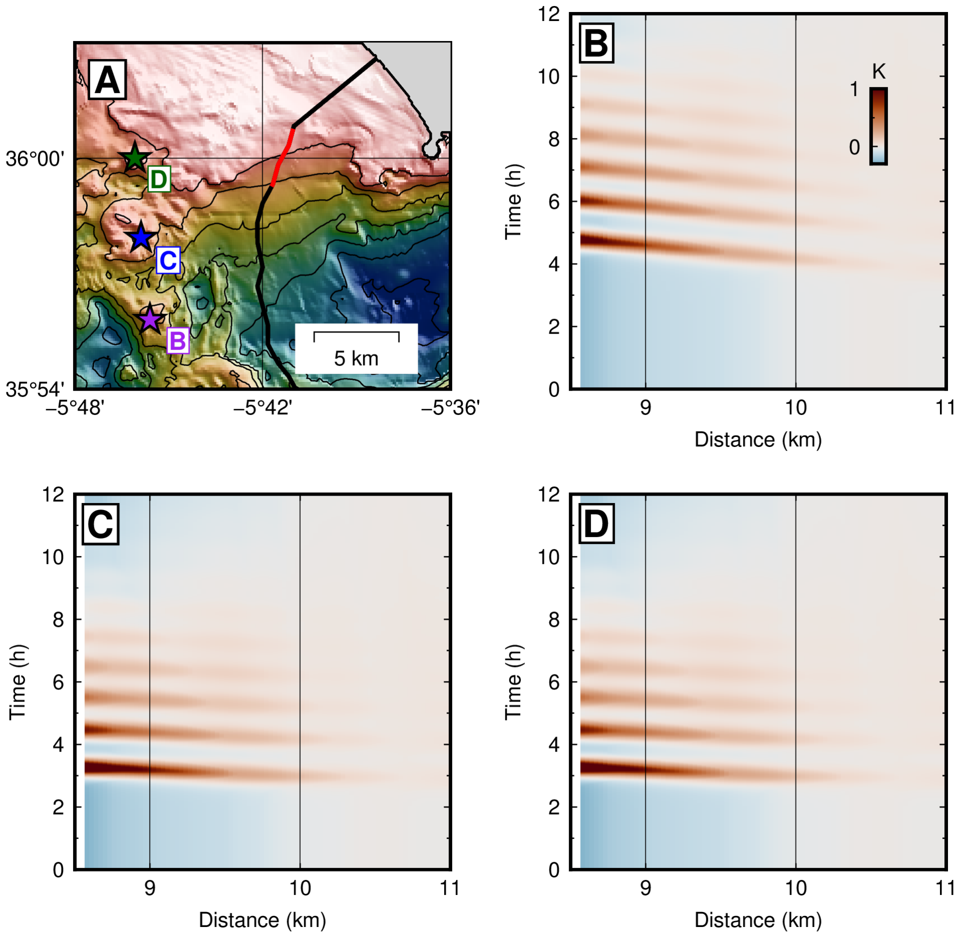

Figure S2. (A) Map of the Camarinal Sill and Strait of Gibraltar cable location, with the segment from Figure 1 of the main text shown in red. (B,C,D) Synthetic data generated using the schematic model of Apel (2003) for different point sources shown in (A), assuming straight-ray propagation. Panel (D) is the same as Figure 1E.

passing wave groups (Figure 2). The validity of this assumption is relatively minor, however, compared to other simplifying assumptions made by this model: any background current is neglected, propagation is assumed along a straight raypath, and the effect of bathymetry on propagation speed is neglected. Consequently, the synthetic data in Figure 2E and S2 should only be considered a schematic representation.

Text S2. Simulation of tidally-driven near-bottom flow

Model configuration and overview

An idealized simulation of tidally-driven turbulence along a sloping bottom in a uniformly-stratified ocean was performed using **flow_solve** (Winters & de la Fuente, 2012), a non-hydrostatic model for process studies of rotating, stratified flows (e.g., Winters (2015); Ulloa et al. (2019); Lelong et al. (2020); Barkan et al. (2017)). We examined the near-boundary flow produced by the reflection of the gravest vertical mode internal tide at a slightly supercritical sloping boundary. The back-reflection of the internal tide at nearly the slope angle produces an oscillatory boundary layer flow characterized by the periodic appearance of sharp up-slope propagating bores. See Winters (2015) for discussion of a similarly-configured simulation, animations of the bore-like features, and a comparison with the observations of van Haren (2006).

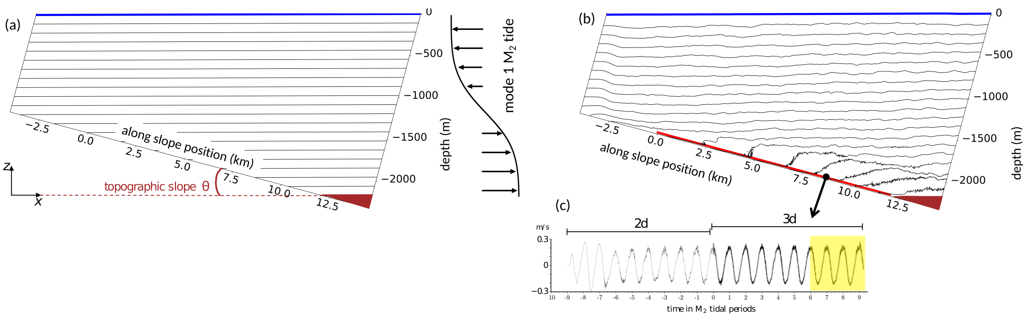

Figure S3. Schematics of the modeling scenario (A) at the initial condition and (B) after 9 tidal periods. The red line indicates the along slope segment analyzed in figure S4. (C) Time series of the x-velocity component within the boundary layer. The three tidal periods shown in Figure 3E and S4 are shaded in yellow.

A schematic of the simulation is shown in Figure S3. The computational domain is tilted to align with the sloping bottom. The domain extends laterally over 21 km to a maximum depth of 2160 m using a spatial resolution of 4.5 m in the tilted coordinate system. The ocean is initialized at rest having a background N value of 1.3×10^{-3} s^{-1}, within the range estimated using WOA18 (Boyer et al., 2018) over 1-2.5 km depths along the submarine cable (1-3 $\times$ 10^{-3} s^{-2}). The incident internal tide is forced at the right boundary at the M_2 frequency with an amplitude of 0.2 m s^{-1} (Figure S3A). The simulation was performed in stages. First, a two-dimensional spin-up run allowed the incident and reflected waves to come into balance near the slope. A snapshot of the flow was then slightly perturbed and extended into three dimensions. The subsequent three-dimensional run allowed for the excitation and evolution of small-scale turbulence in the oscillating boundary layer (Figure S3B). The time series in the schematic shows the x velocity component taken from a point within the boundary layer throughout the simulation stages (Figure S3C). The yellow shading indicates the three tidal periods analyzed in Figure S4. Since this modeling scenario was designed as a laboratory scale experiment, modeling results were re-scaled to be representative of the Gran Canaria DAS observation site using a bottom temperature of 279.3 K, estimated from the WOA18 September climatology extracted for the region.

Implications for interpretation of DAS observations

This idealized modeling scenario yields a pattern of near-bottom temperature that is remarkably similar to that inferred from DAS observations (Figures 3 and 4). Figure S4 plots simulated near-bottom temperature and pressure perturbations (the simulated absolute temperature/pressure with the temporal mean subtracted at each point) along with a representative time series from a fixed location at 6 km (black dashed line). This is the same location plotted in Figure 3E of the main text.

The dominant oscillation is at the M_2 tidal frequency. The slopes of the lines of constant phase (dashed lines) in Figure S4 indicate propagation speeds up the slope. The speed inferred from the pressure signal is about 2.7 m/s, which corresponds to an internal wave at M_2 frequency with a horizontal wavelength of about 120 km. The fixed-point pressure time series is sinusoidal, and the rise and fall of the signal are symmetrical. The bottom pressure is a vertically integrated quantity that is sensitive primarily to the ambient, nearly linear, large-scale internal tide well above the thin bottom boundary layer. In contrast, the temperature signal is dominated by local, nonlinear dynamics within the boundary layer. The slope of the temperature phase lines corresponds to the speed of

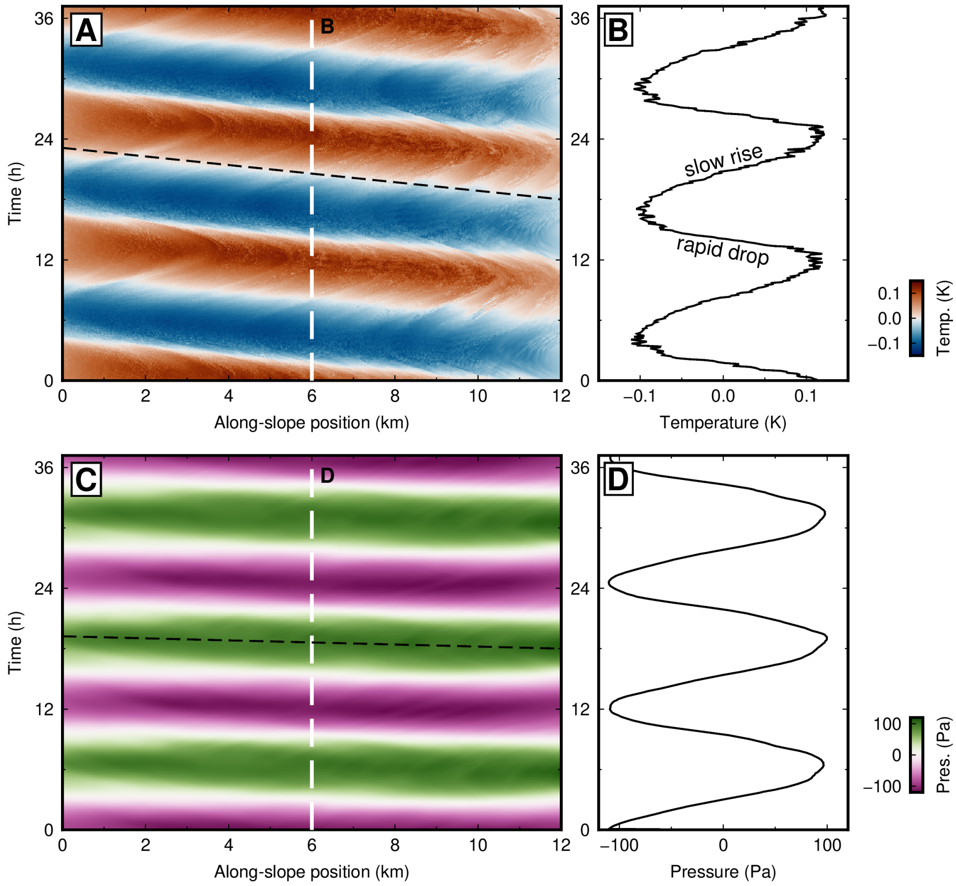

Figure S4. (A) Plot of temperature change as a function of time for a near-bottom slice of the model, indicated with a red line in Figure S3B. (B) Time series of temperature change for a single point from A. (C) Plot of pressure perturbation as a function of time and position, as in A. (D) Time series of pressure perturbation for the same point from C. White dashed lines indicate the position shown in panels B,D and in main text Figure 3E. Black dashed lines indicate the along-slope moveout, with a velocity of about 0.65 m/s for the temperature perturbations in panel A and a velocity of about 2.7 m/s for the pressure perturbations in panel C.

the near-bottom bores as they sweep water up and down the slope. Characteristic of these bores is temporal asymmetry: temperature at a point drops rapidly as the sharp nose of an up-slope bore sweeps cold water upward each tidal cycle. The relaxation phase is significantly slower. The speed of these features inferred from sloping phase is about 0.65 m/s, significantly slower than the phase speed of the internal tide itself. The modeled bore speed is consistent with the estimates of van Haren (2006), who reported significant temporal asymmetry and bore speeds of 0.4–0.5 m/s in the Bay of Biscay. It is also consistent with the DAS estimate (0.5 m/s, shown in Figure 4B of the main text) from a slightly supercritical portion of the Gran Canaria slope.

Text S3. Simple thermal models for the attenuation of temperature by cable construction and burial

To represent the effect of sediment cover or burial on the temperature measured within a cable by DAS, consider heat conduction in a semi-infinite solid $u_t = \kappa u_{zz}$ with uniform thermal diffusivity κ and time-harmonic temperature forcing at the free surface $u(z=0,t) = Ae^{i\omega t}$. This has solution $u(z,t) = Ae^{-z\sqrt{i\omega/\kappa}}e^{i\omega t}$, which is well-known. Treating this as a filter, the temperature response of a point at depth $z = z_0$ relative to the free surface is simply:

$$H(z=z_0,\omega) = \frac{u(z=z_0,\omega)}{u(z=0,\omega)} = e^{-z_0\sqrt{i\omega/\kappa}}.$$

Similarly, to represent the effect of finite cable thickness on the temperature measured internally by DAS, consider heat conduction in a uniform disk $\frac{1}{\kappa}u_t = \frac{1}{r}u_r + u_{rr}$ with time-harmonic temperature forcing at the surface $u(r=R,t) = Ae^{i\omega t}$. This has solution

$$u(r,t) = A\frac{J_0(r\sqrt{-i\omega/\kappa})}{J_0(R\sqrt{-i\omega/\kappa})}e^{i\omega t}$$

for $r \in [0,R]$, where J_0 is a Bessel function of the first kind. The temperature response of a fiber at the center of the cable relative to the exterior is then:

$$H(r=0,\omega) = \frac{u(r=0,\omega)}{u(r=R,\omega)} = \frac{1}{J_0(R\sqrt{-i\omega/\kappa})}.$$

These two models are plotted in Figure S5 for various parameters. Burial beyond a few centimeters strongly attenuates temperature across the internal wave continuum band and tidal periods, using a typical value of thermal diffusivity for marine sediments of 0.2 mm^2/s. For a 50-mm radius cable, a thermal diffusivity similar to common polymers used

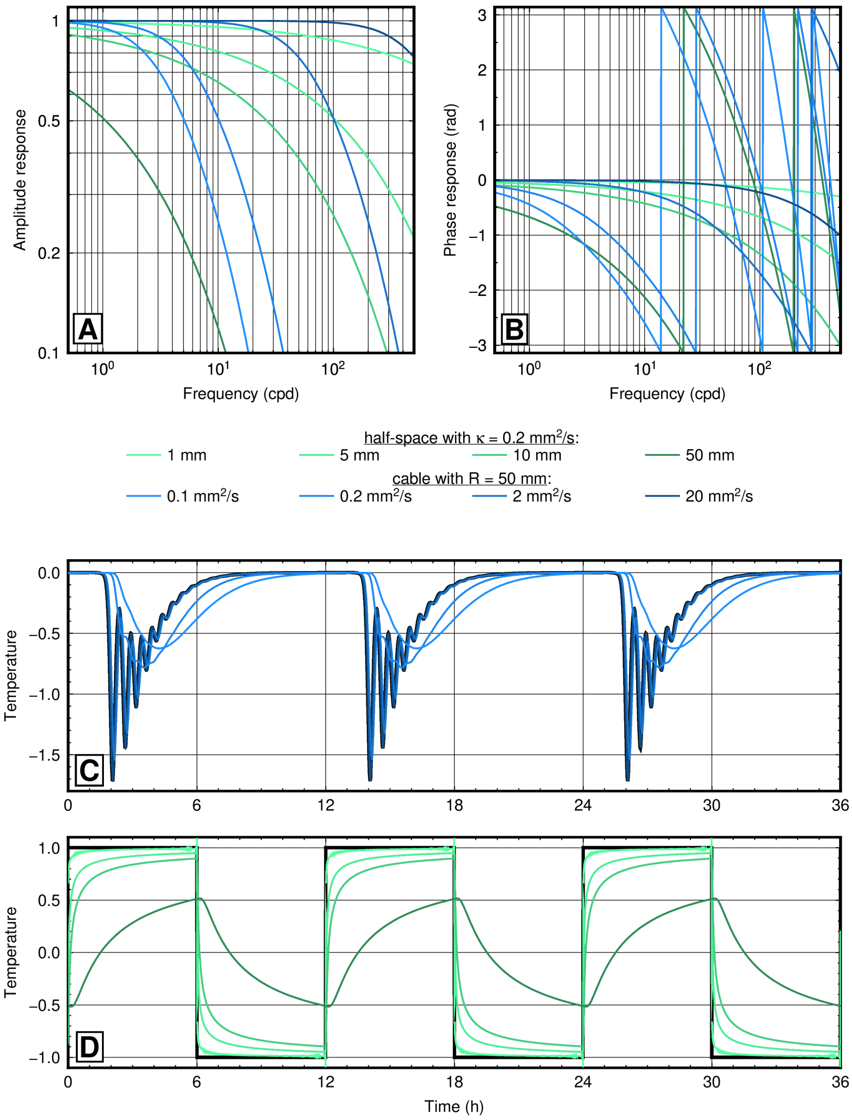

Figure S5. (A) Amplitude and (B) phase response to harmonic temperature forcing at the free surface for a point in a half-space (green) and at the center of a disk (blue) with uniform thermal diffusivity, which are simple models of sediment burial and cable thickness. (C) Example temperature response of a cable with 50-mm radius to internal solitons generated with the "dnoidal" model for different values of thermal diffusivity, analogous to the power cable in the Strait of Gibraltar. (D) Example temperature response of a non-insulating cable to a square wave with burial at various depths in sediment with thermal diffusivity of 0.2 mm^2/s, analogous to the telecommunication cable offshore Gran Canaria.

in cable construction (e.g. rubber, polypropylene, nylon) around 0.1 mm^2/s strongly attenuates temperature across the internal wave continuum band, whereas a value similar to steel or aluminum commonly used for cable armoring around 20 mm^2/s has no effect. Consequently, the exact construction will greatly influence the thermal sensitivity of any cable, though the reduction in sensitivity between armored and unarmored cable is mostly a result of differing thickness.

The difference in response between two cables of identical thermal diffusivity but different diameter to the same forcing is:

$$H(R_1, R_2, \omega) = \frac{J_0(R_1\sqrt{-i\omega/\kappa})}{J_0(R_2\sqrt{-i\omega/\kappa})}$$

as plotted in Figure 4G, comparing the difference in response between single-armored and light-weight protected cable.

Movie S1.

Animation to aid in visualization of along-slope variation in temperature fluctuations associated with nonlinear internal tide dynamics on the slope of Gran Canaria. (Top) Data as shown in Figure 3 of the main text. (Bottom) Along-cable slice in temperature corresponding to the black dashed line above, smoothed with a spatial median filter to suppress small differences in amplitude between adjacent channels. Note that the temperature at each point is the relative temperature with the mean value over a 3-day period subtracted for every channel.

References

Apel, J. R. (2003). A new analytical model for internal solitons in the ocean. *J. Phys. Oceanogr.*, *33*(11), 2247–2269.

Barkan, R., Winters, K. B., & McWilliams, J. C. (2017). Stimulated imbalance and the enhancement of eddy kinetic energy dissipation by internal waves. *J. Phys. Oceanogr.*, *47*, 181-198.

Boyer, T. P., Garcia, H. E., Locarnini, R. A., Zweng, M. M., Mishonov, A. V., Reagan, J. R., … Smolyar, I. V. (2018). *World Ocean Atlas 2018 [September Climatology].* NOAA National Centers for Environmental Information. Dataset.

Brandt, P., Alpers, W., & Backhaus, J. O. (1996). Study of the generation and propagation of internal waves in the strait of gibraltar using a numerical model and synthetic aperture radar images of the european ERS1 satellite. *J. Geophys. Res.*, *101*(C6), 14237–14252.

Cheng, F., Chi, B., Lindsey, N. J., Dawe, T. C., & Ajo-Franklin, J. B. (2021). Utilizing distributed acoustic sensing and ocean bottom fiber optic cables for submarine structural characterization. *Scientific Reports*, *11*(1), 1–14.

Connolly, T. P., & Kirincich, A. R. (2019). High-resolution observations of subsurface fronts and alongshore bottom temperature variability over the inner shelf. *J. Geophys. Res.: Oceans*, *124*, 593–614.

Crawford, W. C., Webb, S. C., & Hildebrand, J. A. (1991). Seafloor compliance observed by long-period pressure and displacement measurements. *J. Geophys. Res.*, *96*(B10), 16151–16160.

Davis, K. A., Arthur, R. S., Reid, E. C., Rogers, J. S., Fringer, O. B., DeCarlo, T. M., & Cohen, A. L. (2020). Fate of internal waves on a shallow shelf. *J. Geophys. Res.: Oceans*, *125*, e2019JC015377.

Egbert, G. D., & Erofeeva, S. Y. (2002). Efficient inverse modeling of barotropic ocean tides. *J. Atmos. Ocean. Technol.*, *19*(2), 183–204.

Egbert, G. D., & Ray, R. (2000). Significant dissipation of tidal energy in the deep ocean inferred from satellite altimeter data. *Nature*, *405*, 775–778.

Egbert, G. D., & Ray, R. D. (2001). Estimates of m2 tidal energy dissipation from topex/poseidon altimeter data. *J. Geophys. Res.*, *106*(C10), 22475–22502.

Farghal, N., Baltay, A., & Langbein, J. (2020). Strain-estimated ground motions associated with recent earthquakes in california. *Bull. Seis. Soc. Am.*, *110*(6), 2766–2776.

Fernandez-Ruiz, M. R., Costa, L., & Martins, H. F. (2019). Distributed acoustic sensing using chirped-pulse phase-sensitive OTDR technology. *Sensors*, *19*(20), 4368.

Fernandez-Ruiz, M. R., Martins, H. F., Costa, L., Martin-Lopez, S., & Gonzalez-Herraez, M. (2018). Steady-sensitivity distributed acoustic sensors. *J. Light. Technol.*, *36*, 5690–5696.

Fernandez-Ruiz, M. R., Soto, M. A., Williams, E. F., Martin-Lopez, S., Zhan, Z., Gonzalez-Herraez, M., & Martins, H. F. (2020). Distributed acoustic sensing for seismic activity monitoring. *APL Photonics*, *5*(3), 030901.

Garrett, C., & Munk, W. (1972). Oceanic mixing by breaking internal waves. *Deep Sea Research and Oceanographic Abstracts*, *19*, 823–832.

Ide, S., Araki, E., & Matsumoto, H. (2021). Very broadband strain-rate measurements along a submarine fiber-optic cable off Cape Muroto, Nankai subduction zone, Japan. *Earth, Planets, Space*, *73*(63).

Kinder, T. H., & Bryden, H. L. (1987). The 1985–1986 Gibraltar Experiment: Data collection and preliminary results. *Eos, Trans. Am. Geophys. Union*, *68*, 786–795.

Klymak, J. M., Alford, M. H., Pinkel, R., Lien, R., Yang, Y. J., & Tang, T. (2011). The breaking and scattering of the internal tide on a continental slope. *J. Phys. Oceanogr.*, *41*, 926–945.

Koyamada, Y., Imahama, M., Kubota, K., & Hogari, K. (2009). Fiber-optic distributed strain and temperature sensing with very high measurand resolution over long range using coherent OTDR. *J. Lightwave Technol.*, *27*, 1142–1146.

Kunze, E. (2017). Internal-wave-driven mixing: Global geography and budgets. *J. Phys. Oceanogr.*, *47*(6), 1325–1345.

Kunze, E., MacKay, C., McPhee-Shaw, E. E., Morrice, K., Girton, J. B., & Terker, S. R. (2012). Turbulent mixing and exchange with interior waters on sloping boundaries. *J. Phys. Oceanogr.*, *42*, 910–927.

Ledwell, J. R., Montgomery, E. T., Polzin, K. L., St. Laurent, L. C., Schmitt, R. W., & Toole, J. M. (2000). Evidence for enhanced mixing over rough topography in the abyssal ocean. *Nature*, *403*, 179–182.

Lelong, M.-P., Cuypers, Y., & Bouruet-Aubertot, P. (2020). Near-Inertial Energy Propagation inside a Mediterranean Anticyclonic Eddy. *Journal of Physical Oceanography*, *50*(8), 2271 - 2288. doi: 10.1175/JPO-D-19-0211.1

Li, J., & Zhang, M. (2022). Physics and applications of raman distributed optical fiber sensing. *Light Sci. Appl.*, *11*(128).

Lindsey, N. J., Dawe, T. C., & Ajo-Franklin, J. B. (2019). Illuminating seafloor faults and ocean dynamics with dark fiber distributed acoustic sensing. *Science*, *366*(6469), 1103–1107.

Lindsey, N. J., & Martin, E. R. (2021). Fiber-optic seismology. *Ann. Rev. Earth Planet. Sci.*, *49*, 309–336.

Mecozzi, A., Cantono, M., Castellanos, J. C., Kamalov, V., Muller, R., & Zhan, Z. (2021). Polarization sensing using submarine optical cables. *Optica*, *8*(6), 788–795.

Moum, J. N., Caldwell, D. R., Nash, J. D., & Gunderson, G. D. (2002). Observations of boundary mixing over the continental slope. *J. Phys. Oceanogr.*, *32*(7), 2113–2130.

Moum, J. N., & Smyth, W. D. (2006). The pressure disturbance of a nonlinear internal wave train. *J. Fluid Mech.*, *558*, 153–177.

Munk, W. H. (1966). Abyssal recipes. *Deep-Sea Research*, *13*, 707–730.

Pastor-Graells, J., Martins, H., Garcia-Ruiz, A., Martin-Lopez, S., & Gonzalez-Herraez, M. (2016). Single-shot distributed temperature and strain tracking using direct detection phase-sensitive OTDR with chirped pulse. *Optics Express*, *24*, 13121–13133.

Polzin, K., Toole, J., Ledwell, J., & Schmitt, R. (1997). Spatial variability of turbulent mixing in the abyssal ocean. *Science*, *276*, 93–96.

Rudnick, D. L., Boyd, T. J., Brainard, R. E., Carter, G. S., Egbert, G. D., Gregg, M. C., … Sanford, T. B. (2003). From tides to mixing along the Hawaiian ridge. *Science*, *301*, 355–357.

Sidenko, E., Tertyshnikov, K., Lebedev, M., & Pevzner, R. (2022). Experimental study of temperature change effect on distributed acoustic sensing continuous measurements. *Geophysics*, *87*(3), D111–D122.

Sinnett, G., Davis, K. A., Lucas, A. J., Giddings, S. N., Reid, E., Harvey, M. E., & Stokes, I. (2020). Distributed temperature sensing for oceanographic applications. *J. Atmos. Ocean. Tech.*, *37*, 1987–1997.

Sladen, A., Rivet, D., Ampuero, J.-P., de Barros, L., Hello, Y., Calbris, G., & Lamare, P. (2019). Distributed sensing of earthquakes and ocean-solid earth interactions on seafloor telecom cables. *Nature Comms.*, *10*(1), 1–8.

St. Laurent, L., & Garrett, C. (2002). The role of internal tides in mixing the deep ocean. *J. Phys. Oceangr.*, *32*, 2882–2899.

Toole, J. M., Schmitt, R. W., & Polzin, K. L. (1994). Estimates of diapycnal mixing in the abyssal ocean. *Science*, *264*(5162), 1120-1123.

Ugalde, A., Becerril, C., Villaseñor, A., Ranero, C. R., Fernández-Ruiz, M. R., Martin-Lopez, S., … Martins, H. F. (2022). Noise levels and signals observed on submarine fibers in the Canary Islands using DAS. *Seismol. Res. Lett.*, *93*(1), 351–363.

Ulloa, H. N., Winters, K. B., Wüest, A., & Bouffard, D. (2019). Differential heating drives downslope flows that accelerate mixed-layer warming in ice-covered waters. *Geophysical Research Letters*, *46*(23), 13872-13882. doi: https://doi.org/10.1029/2019GL085258

van Haren, H. (2006). Nonlinear motions at the internal tide source. *Geophys. Res. Lett.*, *33*, L11605.

van Haren, H., Cimatoribus, A., & Gostiaux, L. (2015). Where large deep-ocean waves break. *Geophys. Res. Lett.*, *42*, 2351–2357.

van Haren, H., & Gostiaux, L. (2010). A deep-ocean Kelvin-Helmholtz billow train. *Geophys. Res. Lett.*, *37*, L03605.

van Haren, H., & Gostiaux, L. (2012). Detailed internal wave mixing above a deep-ocean slope. *J. Mar. Res.*, *70*, 173–197.

van Haren, H., Maas, L., & van Aken, H. (2002). On the nature of internal wave spectra near a continental slope. *Geophys. Res. Lett.*, *29*(12), 1615.

Vazquez, A., Bruno, M., Izquierdo, A., Macias, D., & Ruiz-Canavate, A. (2008). Meteorologically forced subinertial flows and internal wave generation at the main sill of the Strait of Gibraltar. *Deep Sea Res. I*, *55*(10), 1277–1283.

Waterhouse, A. F., MacKinnon, J. A., Nash, J. D., Alford, M. H., Kunze, E., Simmons, H. L., … Lee, C. M. (2014). Global patterns of diapycnal mixing from measurements of the turbulent dissipation rate. *J. Phys. Oceanogr.*, *44*(7), 1854–1872.

Watson, G., & Robsinson, I. S. (1990). A study of internal wave propagation in the strait of gibraltar using shore-based marine radar images. *J. Phys. Oceanogr.*, *20*, 374—395.

Williams, E. F., Fernandez-Ruiz, M. R., Magalhaes, R., Vanthillo, R., Zhan, Z., Gonzalez-Herraez, M., & Martins, H. F. (2019). Distributed sensing of microseisms and teleseisms with submarine dark fibers. *Nature Communications*, *10*(5778), 1-16.

Williams, E. F., Fernandez-Ruiz, M. R., Magalhaes, R., Vanthillo, R., Zhan, Z., Gonzalez-Herraez, M., & Martins, H. F. (2021). Scholte wave inversion and passive source imaging with ocean-bottom DAS. *The Leading Edge*, *40*(8), 576–583.

Williams, E. F., Zhan, Z., Martins, H. F., Fernandez-Ruiz, M. R., Martin-Lopez, S., Gonzalez-Herraez, M., & Callies, J. (2022). Surface gravity wave interferometry and ocean current monitoring with ocean-bottom DAS. *J. Geophys. Res.: Oceans*, *127*, e2021JC018375.

Winters, K. B. (2015). Tidally driven mixing and dissipation in the stratified boundary layer above steep submarine topography. *Geophys. Res. Lett.*, *42*, 7123—7130.

Winters, K. B., & de la Fuente, A. (2012). Modelling rotating stratified flows at laboratory-scale using spectrally-based DNS. *Ocean Modelling*, *49-50*, 47-59. doi: https://doi.org/10.1016/j.ocemod.2012.04.001

Ziegenbein, J. (1969). Short internal waves in the Strait of Gibraltar. *Deep Sea Res.*, *16*, 479–487.

Ziegenbein, J. (1970). Spatial observations of short internal waves in the Strait of Gibraltar. *Deep Sea Res.*, *17*(5), 867–875.

Zumberge, M. A., Hatfield, W., & Wyatt, F. K. (2018). Measuring seafloor strain with an optical fiber interferometer. *Earth and Space Science*, *5*, 371—379.